Switching Terahertz Waves using Exceptional Points

Xu-Lin Zhang,[1,2] Xi-Bin Wang,[2,3] and C. T. Chan[1,*]

[1]*Department of Physics, The Hong Kong University of Science and Technology, Clear Water Bay, Hong Kong, China*

[2]*State Key Laboratory of Integrated Optoelectronics, College of Electronic Science and Engineering, Jilin University, Changchun, China*

[3]*Department of Electronic Engineering, City University of Hong Kong, 83 Tat Chee Ave., Hong Kong, China*

(Received 20 March 2018; revised manuscript received 11 June 2018; published 21 September 2018)

Exceptional points (EPs) are non-Hermitian degeneracies that can enable various intriguing applications such as enhanced sensing and asymmetric mode switching. Here, we theoretically propose the design of a 1×2 terahertz switch by employing the topological structure of the energy surfaces (i.e., eigenvalue distributions in a two-variable parameter space) near an EP. The switch consists of a pair of terahertz waveguides, one of which has a monolayer graphene laid on the bottom. The wave transmission through the system can be understood by considering an adiabatic trajectory on self-intersecting Riemann sheets due to the existence of an EP. The trajectory can be tuned by changing the chemical potential of graphene, and as a result, we can choose in which waveguide the power exits to achieve the switching functionality. The physics behind the switch lies in the fact that the trajectories on different sides of the EP lead to different final states due to the unique topological structure of energy surfaces near the EP. We perform numerical simulations to optimize the performance of the terahertz switch.

DOI: 10.1103/PhysRevApplied.10.034045

I. INTRODUCTION

Exceptional points (EPs) are degeneracies in non-Hermitian systems that have attracted much research interests in recent years [1–4]. The simplest model that exhibits an EP is a parity-time-symmetric (PT-symmetric) two-oscillator system with balanced gain and loss (i.e., non-Hermiticity). When the gain/loss is equal to the intrinsic coupling between the two oscillators, both the eigenvalues and eigenvectors of the system coalesce at an EP. An interesting property of the EP is the topological structure of the energy surfaces [5], i.e., the eigenvalue distributions in a parameter space, which can give rise to unusual properties. For example, adiabatically encircling an EP in a two-variable parameter space can result in an eigenstate exchange due to the unique topological structure [6,7]. While many EP-related phenomena are studied using two-state systems, higher order EPs have also been studied and shown to exhibit an even more complex topological structure of energy surfaces [8,9]. The intriguing physics of EPs have given rise to a variety of fascinating and counterintuitive phenomena [10–17].

From a theory point of view, non-Hermitian systems are more challenging to handle mathematically, but non-Hermiticity gives an extra degree of freedom that facilitates the development of new applications. For example, the topological structure associated with the EP has been utilized to realize asymmetric mode switching by dynamically encircling the EP [18–20]. Enhanced sensitivity has been achieved near the EP by employing the square-/cube-root singularity near a second-/third-order EP [21–23]. Some features of PT-symmetry have been employed to design optical switches [24,25]. There are also applications in the fields of wireless power transfer [26], lasing [27,28], and metasurfaces [29], as well as molecular physics [30,31]. We see that non-Hermitian systems can realize some functionalities that are difficult to achieve in Hermitian systems due to their unique characteristics.

Terahertz technologies have become increasingly important in recent years due to the very diverse applications [32,33]. For terahertz communication systems, a key component is the terahertz switch, which is typically realized using waveguide structures for the sake of enhanced light-matter interaction [34]. Different switching principles have been used, ranging from manipulating the bandgap of photonic crystals using the electro-optical effect [35,36], magneto-optical effect [37], and nonlinear effect [38], and tuning the loss of graphene [34,39,40], as well as employing the interference effect by adding a control wave [41]. In this work, we make use of the topological features of the energy surfaces around a second-order EP to design a 1×2 terahertz switch. We first study the eigenmodes of a pair of terahertz waveguides with a graphene stripe attached to one of them. We consider a two-variable parameter space

*phchan@ust.hk

and the eigenmode dispersions in the parameter space form two self-intersecting Riemann sheets exhibiting an EP. We consider the dynamical evolution that follows a particular trajectory on the Riemann sheets and the designed trajectory can be tuned by changing the chemical potential of graphene. We find that although the starting state of the trajectory is localized in the same waveguide, the final state can be different when the trajectory in parameter space lies on different sides of the EP. This path-dependence phenomenon is then used to design the 1×2 terahertz switch in which the chemical potential of graphene can be used to pick the waveguide that carries the output signal. We perform numerical simulations to investigate the performance of the switch. We also study the dependence of the performance on the system parameters to optimize the device performance.

II. PHYSICS BEHIND THE TERAHERTZ SWITCH

We start by showing the design principle of the 1×2 terahertz switch using the topological structure of the energy surfaces around an EP. Figure 1(a) illustrates the cross section of a pair of terahertz waveguides placed on a substrate. The refractive indices of the waveguides and the substrate are set to be 1.6 and 1.4, respectively, at the frequency of interest (approximately 0.5 THz). In the experiment, the waveguide and substrate can be made of polymethyl methacrylate (PMMA) and Teflon, respectively [42]. The widths of the two waveguides are W_1 and W_2, respectively. Both waveguides have the same height H, and they are separated by a gap distance of g. We introduce loss into the system by placing a monolayer graphene with a width of w at the bottom of waveguide-1, as depicted by the red line in Fig. 1(a). The surface conductivity of the graphene stripe can be determined by the Kubo formula including both the intraband and interband contributions [43]. At terahertz frequencies, the interband contribution is very small compared to the intraband contribution so that the surface conductivity takes the form

$$\sigma_S = \frac{ie^2 k_B T}{\pi \hbar^2 (\omega + i\tau^{-1})} \left\{ \frac{\mu_c}{k_B T} + 2 \ln \left[1 + \exp\left(-\frac{\mu_c}{k_B T} \right) \right] \right\}, \tag{1}$$

where e, k_B, T, τ, and μ_c represent the electron charge, Boltzmann constant, temperature, relaxation time, and chemical potential, respectively. Figure 1(b) plots the calculated surface conductivity as a function of the chemical potential at 0.5 THz, where we fix $T = 300$ K and $\tau = 10^{-13}$ s. We note that by increasing the chemical potential, the surface conductivity increases, which is associated with a larger ohmic loss in graphene. In practice, the chemical potential of graphene can be tuned using various schemes including electrical gating, electrothermal effect, photothermal effect, and optical excitation [44].

The loss of graphene plays a key role in manipulating the EP in our system. To show this point, we study the eigenmodes of the system, which give the steady form of the wave propagation along the z axis. The eigenmodes are confined inside the waveguide by total internal reflection, and they can be obtained by solving the Maxwell equations,

$$\nabla \times \nabla \times \vec{E} = \frac{\omega^2}{c^2} n^2 \vec{E}, \tag{2}$$

where c is the speed of light in vacuum and n is the refractive index of the material, subject to the boundary conditions. The magnetic fields are related to the electric fields via $\vec{H} = \nabla \times \vec{E}/(i\omega\mu_0)$, where μ_0 is the free space permeability. Each eigenmode has a propagation constant β and the electric fields can be written as $\vec{E}(x,y)\exp(i\beta z)$. We only need to solve the transverse component $\vec{E}_t(x,y)$ since the longitudinal component $E_z(x,y)$ can be determined from the transverse one. In the proposed system, each single waveguide is designed to support only two eigenmodes, i.e., one with electric fields polarized mainly along the x axis while the other one is polarized along the y axis. We label them as x polarized and y polarized modes, respectively. Since one component of the transverse electric field dominates over the other one, we can use the scale field approximation to obtain the eigenvalue equation as, taking the x polarized modes, for example [45],

$$\nabla_t^2 E_x(x,y) + \frac{\omega^2}{c^2} n^2(x,y) E_x(x,y) = \beta^2 E_x(x,y), \tag{3}$$

where $\nabla_t = \hat{x}(\partial/\partial x) + \hat{y}(\partial/\partial y) = \nabla - i\beta\hat{z}$. The propagation constant and eigenfields can be obtained by solving Eq. (3) and the corresponding boundary conditions. However, we cannot obtain analytical solutions for rectangular waveguides without approximations. We use a numerical finite element solver COMSOL Multiphysics [46]. The effective mode index n_{eff}, defined as $n_{\text{eff}} = \beta/k_0$ with $k_0 = 2\pi/\lambda$, can be calculated using the eigenmode analysis study in the electromagnetic waves module, in which Eq. (3) associated with boundary conditions is solved on the cross section of the waveguide for a given frequency.

We show the calculated effective mode index of the eigenmodes as a function of the chemical potential in Figs. 1(c) and 1(d), respectively, for the x polarized and y polarized modes. In the simulation, the structural parameters are $W_1 = W_2 = 0.7$ mm, $H = 0.35$ mm, $g = 0.1$ mm, and $w = 0.1$ mm, and the frequency is 0.5 THz. From Fig. 1(c), we see that the x polarized modes exhibit typical EP characteristics, i.e., the real parts of the effective index approach each other whereas the imaginary parts repel each other as the chemical potential increases. The x component electric field distributions of the eigenmodes are shown at $\mu_c = 0$ and 0.4 eV in the inset of Fig. 1(c). It is clear that when the loss of graphene is

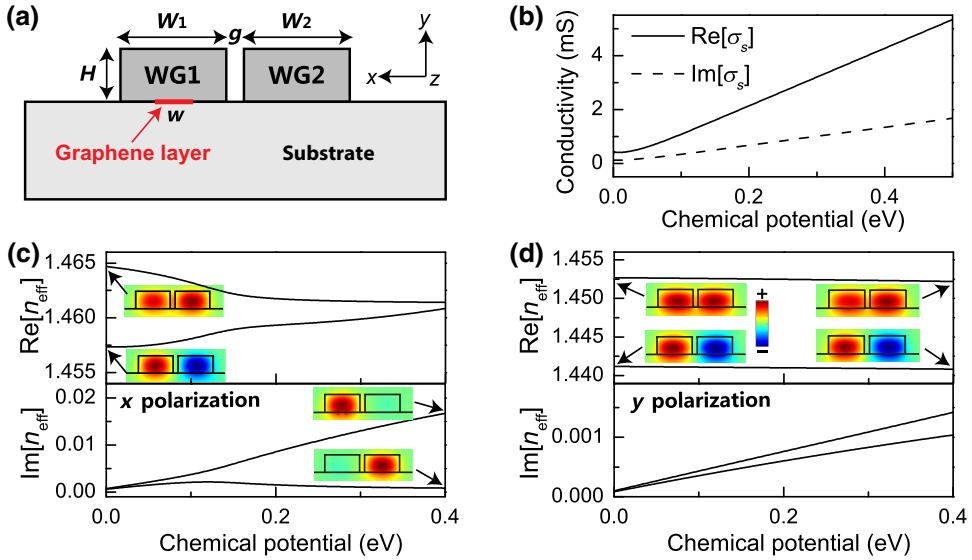

FIG. 1. (a) Cross section of a pair of waveguides on a substrate. The red line illustrates a graphene stripe placed between waveguide-1 and the substrate. The symbols W_1, W_2, H, g, and w denote the width of waveguide-1, the width of waveguide-2, the waveguide height, the gap distance between the two waveguides, and the width of the graphene stripe. The waveguides and the substrate have the refractive indices of 1.6 and 1.4, respectively, and could be made of PMMA and Teflon. The background is air. (b) Surface conductivity of graphene as a function of chemical potential at the frequency of 0.5 THz. (c) Calculated effective mode index of x polarized modes in the waveguide system as a function of the chemical potential. (d) Same as (c) except for y polarized modes. The insets of (c) and (d) show the corresponding x and y components electric fields of the eigenmodes, respectively, where the red/blue color corresponds to positive/negative values. In the simulations, the system parameters are $W_1 = W_2 = 0.7$ mm, $H = 0.35$ mm, $g = 0.1$ mm, and $w = 0.1$ mm. The frequency is 0.5 THz.

very small ($\mu_c \sim 0$ eV), one eigenmode is symmetric while the other one is antisymmetric. At $\mu_c = 0.4$ eV, in contrast, the field of one eigenmode is mainly localized in waveguide-1 while that of the other eigenmode is localized in waveguide-2. This shows that the system enters the broken symmetry phase when the differential loss becomes larger compared to the coupling [10]. The situation is quite different for y polarized modes for which the polarized direction is orthogonal to the graphene stripe so that the eigenmodes hardly interact with graphene [43]. As a result, the eigenmodes exhibit almost no dispersion in the parameter range shown in Fig. 1(d).

While EP-like behavior is evident, strictly speaking, the EP for the x polarized modes does not appear in Fig. 1(c). This is because only one waveguide is attached with the graphene stripe and this causes a detuning of the effective index eigenvalues. To access the EP, we need to change another system parameter such as the width of waveguide-2 to compensate for the detuning. Together with the chemical potential, we now have a μ_c-W_2 two-variable parameter space. We calculate the effective mode index of the eigenmodes as a function of the two parameters. The calculated dispersion relations of the x polarized modes are plotted as Riemann sheets [18] in Figs. 2(a) and 2(b) for the real parts and imaginary parts, respectively. The red/blue sheet corresponds to the eigenmode with higher/lower loss. We find an EP located at $\mu_{c,\mathrm{EP}} = 0.143$ eV and $W_{2,\mathrm{EP}} = 0.687$ mm, where both the real parts and imaginary parts of the eigenvalues coalesce. The self-intersecting Riemann sheets near the EP can induce interesting dynamical properties such as eigenmode exchange when the system dynamics follow a trajectory encircling the EP [6,7]. Figures 2(c) and 2(d) plot the Riemann sheets of the y polarized modes and no EP can be found as the modes are insensitive to the loss of the graphene stripe.

We design a terahertz switch based on the Riemann sheets of x polarized modes. Manipulating the Riemann sheets to design a dynamical process was first proposed in Refs. [18] and [19], where asymmetric mode switching was realized for symmetric and antisymmetric modes by introducing a loop trajectory enclosing the EP. As we aim to design a terahertz switch, a line trajectory perpendicular to the μ_c axis is introduced, with the starting point at $W_2 = W_1 - \Delta W$ and the end point at $W_2 = W_1 + \Delta W$, where the eigenmodes are symmetry-broken modes (or localized modes, see Fig. 3). The starting point is fixed on the lower-loss sheet (the blue sheet in Fig. 2). It is then noted that the final states are different when the trajectory lies on different sides of the EP if the evolution process is adiabatic. One case is shown by the yellow line [see Fig. 2(b)] which is "before" the emergence of the EP (i.e., $\mu_c < \mu_{c,\mathrm{EP}}$) as the loss is small. The state can climb up to the higher-loss sheet (the red sheet) via the symmetric phase, which is also a branch cut of the Riemann surface

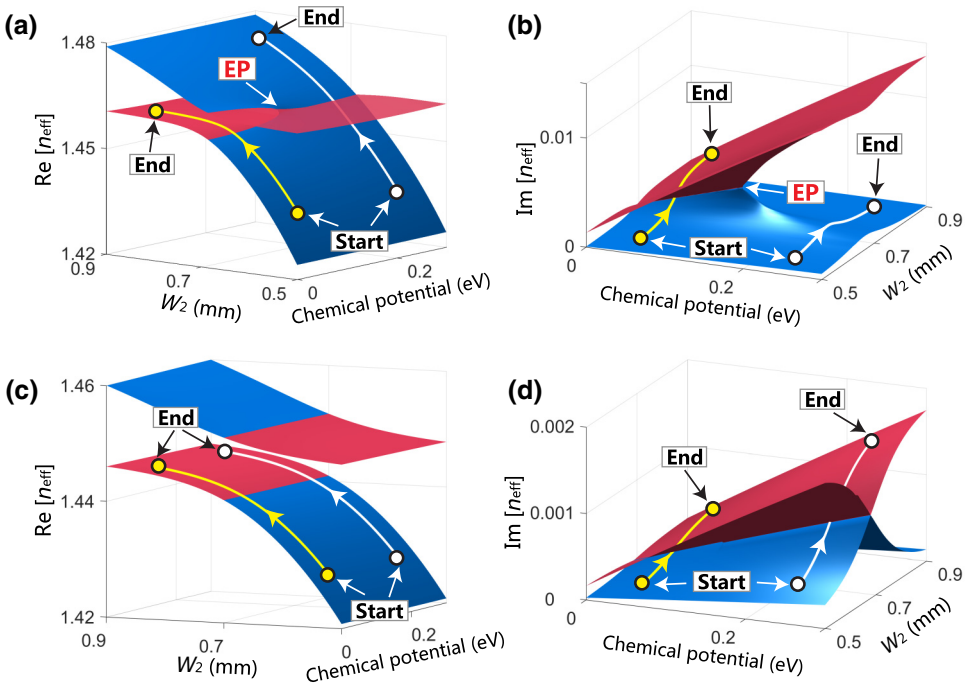

FIG. 2. (a) Real and (b) imaginary parts of the effective mode index of x polarized eigenmodes as a function of μ_c and W_2. An EP is located at $\mu_{c,\mathrm{EP}} = 0.143$ eV and $W_{2,\mathrm{EP}} = 0.687$ mm. The yellow and white lines show two trajectories on the Riemann sheets with $\mu_c = 0.05$ and 0.25 eV, respectively, with the end state on the higher-loss sheet (red sheet) and lower-loss sheet (blue sheet), although for both trajectories the starting state lies on the lower-loss sheet. Items shown in (c) and (d) are the same as those in (a) and (b) except for y polarized modes, of which the energy surfaces do not possess an EP.

where the imaginary parts of the eigenvalues coalesce. As a result, the process ends up with a final state on the higher-loss sheet. In another case, the trajectory is "after" the emergence of the EP (i.e., $\mu_c > \mu_{c,\mathrm{EP}}$) as marked by the white line [see Fig. 2(b)], which passes through the broken phase where the real parts of the eigenvalues coalesce [also see Fig. 2(a)]. The final state remains on the lower-loss sheet since "after" the EP, there is no branch cut that connects the lower-loss sheet and higher-loss sheet.

The yellow and white trajectories can lead to different mode conversion behaviors. To show this point, we plot the evolution of the eigenfield distributions along the two trajectories in the parameter space in Fig. 3. By introducing a large detuning ΔW (e.g., at the starting/end point), the energy of the eigenmode would be mainly localized in the lossy waveguide-1/lossless waveguide-2 when the eigenstate lies on the higher-loss red sheet/lower-loss blue sheet. More specifically, the yellow trajectory shows the process by which the energy in waveguide-2 (starting point) gradually transfers to waveguide-1 (end point) via the symmetric phase/branch cut (see the dashed line). In contrast, the white trajectory shows a different behavior by which the power flow is propagating in waveguide-2 for the whole process. We note that although the input states of the two trajectories both lie on the lower-loss sheet associated with the energy localized in waveguide-2, the final states are completely different in the sense that they stay on different Riemann sheets with the energy localized in different waveguides. The discrepancy is due to the topological structure of the energy landscape around the EP.

These two different state evolution processes can be employed to design a terahertz switch. A schematic diagram of the design is illustrated in Fig. 4. Terahertz waves with a power of P_0 are injected from waveguide-2 in region I. The key component of the system is region II in which the wave transmission through it follows the trajectory on the Riemann sheets designed above [see Figs. 2(a) and 2(b)]. More specifically, waveguide-1 with graphene attached has a uniform width W_1 whereas the width of waveguide-2 changes linearly from $W_1 - \Delta W$ (left side) to $W_1 + \Delta W$ (right side). The wave transmission can be manipulated by tuning the chemical potential of graphene. When the chemical potential is lower than $\mu_{c,\mathrm{EP}}$, the energy of the terahertz wave should be concentrated in the lossy waveguide-1 (see the yellow trajectory in Fig. 3) at the end of region II. As a result, the output power would satisfy $P_1 > P_2$ in region III. When the chemical potential is larger than $\mu_{c,\mathrm{EP}}$, the power flow of the final state is mainly propagating in the lossless waveguide-2 (see the white trajectory in Fig. 3). We then have $P_2 > P_1$ in region III. By using an external parameter to tune the chemical potential of graphene, we can manipulate the trajectory of

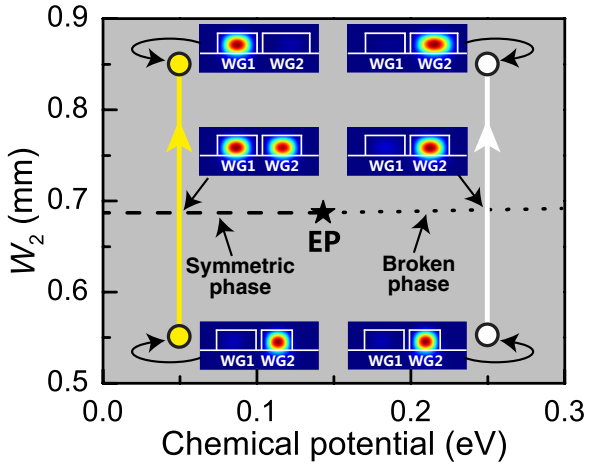

FIG. 3. Parameter space and designed trajectories for the x polarized modes. The star marks the EP, and the dashed and dotted lines represent the symmetric phase and broken phase, corresponding to the coalescing of imaginary parts and real parts of the eigenvalues, respectively. The inset shows the evolution of the eigenfield distributions (z component power flow) along the yellow and white trajectories with $\mu_c = 0.05$ and 0.25 eV, respectively.

the state on the Riemann sheets and thus control the final state, i.e., the waveguide in which the power goes out in region III. This is the switching functionality we achieve in our system. The first design of an optical switch using the concept of PT-symmetry was proposed in Ref. [24]. Our design is different in the sense that we employ the topological structure of energy surfaces around the EP to design the switch. Our state is adiabatically evolving on the Riemann sheets while the state in Ref. [24] is fixed at one point of the parameter space.

It is quite well known that in a dynamical process, nonadiabatic transitions may occur when the state evolves on the higher-loss Riemann sheet [18,20,47,48]. We note that nearly half of the yellow trajectory lies on the red sheet. But nonadiabatic transitions will not occur in our system since we will show in the following device design that for the yellow trajectory, the loss of the graphene stripe should be as small as possible in order to achieve a good device performance. The relatively small loss is not sufficient to induce nonadiabatic transitions. In fact, the ideal working condition for the yellow trajectory is that the system has no loss so that nonadiabatic transitions will never occur.

III. PERFORMANCE OF THE TERAHERTZ SWITCH

We perform numerical simulations to investigate the performance of the designed terahertz switch. Near the interface between region I and region II, the eigenmodes in region II are symmetry-broken modes (see Fig. 3) since waveguide-1 and waveguide-2 have a detuning (i.e., $W_1 \neq W_2$). As a result, the single mode propagating in region I can couple to the eigenmode localized in waveguide-2 in region II very efficiently. We only consider region II in numerical simulations. In the simulations, we first solve the eigenmode field distributions at the two interfaces using the boundary mode analysis study in the electromagnetic waves module of COMSOL Multiphysics [46]. The eigenfields are then used as boundary conditions and the wave transmission in the system is calculated using the frequency domain study. We define two conversion efficiencies $\eta_1 = P_1/P_0$ and $\eta_2 = P_2/P_0$, where P_1 and P_2 are calculated by integrating the power flow (or Poynting vector) in the whole cross section of waveguide-1 and waveguide-2, respectively, at the interface between region II and region III. The system parameters are chosen to be $L = 60$ mm and $\Delta W = 0.1$ mm. Figure 5(a) shows the conversion efficiencies as a function of the chemical potential for x polarized modes, where the vertical dashed line marks the position of the EP ($\mu_{c,\mathrm{EP}} = 0.143$ eV). We note that when $\mu_c = 0$, P_1 dominates the output power, indicating that the power flow transfers from waveguide-2 to waveguide-1 in the evolution process. When the chemical potential is larger than $\mu_{c,\mathrm{EP}}$, the output is dominated by P_2. We also plot $\eta_1 + \eta_2$ as a function of μ_c. The total conversion efficiency is found to decay at first, but then increase again, with the inflection point around the EP. This is a phenomenon of loss-induced transmission enhancement.

The phenomenon can be understood from the simulated z component power flow distributions for x polarized modes which are shown in Figs. 6(a) and 6(b) with $\mu_c = 0$ and 0.5 eV, respectively. When the loss is small [Fig. 6(a)], we can clearly see a transfer of the power flow at the center of the system ($z = \sim 30$ mm) because there is a branch cut for the state to climb up to the higher-loss sheet/waveguide-1 [see the yellow line in Fig. 2(b) for intuitive understanding although the values of μ_c are not exactly the same]. The total transmission decays as the graphene loss increases. Increasing the loss further leads to the EP, after which the state can no long climb up to the higher-loss sheet [see the white line in Fig. 2(b)] and therefore the total transmission increases again. Figure 6(b) shows such a case for which the wave propagates mainly in waveguide-2 for the whole process. The phenomenon of loss-induced transmission enhancement was also observed in Ref. [10], but the mechanisms are different. The waveguides in Ref. [10] have the same dimensions along the waveguiding direction so that the corresponding trajectory is a point in the parameter space. When the loss is small, the eigenmodes are symmetric and antisymmetric modes which cannot be used directly for switching functionality. In our design, a detuning is introduced at the input and output of Region II (i.e., $W_1 \neq W_2$), which ensures the eigenmodes to be symmetry-broken modes. We also design a line trajectory and make use of the topological structure

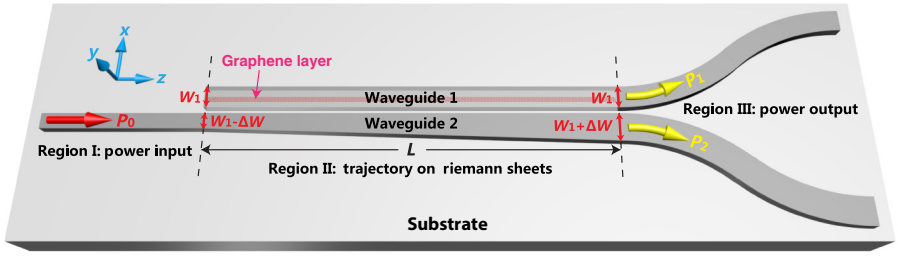

FIG. 4. Schematic diagram of the terahertz switch. The terahertz wave with a power of P_0 is injected from waveguide-2 in region I. Region II is the key region where waveguide-I has a uniform width W_1 while the width of waveguide-2 changes linearly from $W_1 - \Delta W$ (left side) to $W_1 + \Delta W$ (right side). The red region in waveguide-1 depicts a graphene stripe with a width of w [see Fig. 1(a) for detailed position]. Region III is the output region in which the output powers in waveguide-1 and waveguide-2 are denoted by P_1 and P_2, respectively. The system is designed to work at 0.5 THz. The optimized structural parameters are $W_1 = 0.7$ mm, $\Delta W = 0.1$ mm, $H = 0.35$ mm, $g = 0.1$ mm, $w = 0.1$ mm, and $L = 60$ mm.

of energy surfaces around the EP to realize the switching functionality.

The conversion efficiencies for y polarized modes are also calculated in Fig. 5(b) for comparison. As the corresponding energy surfaces do not possess an EP [see Figs. 2(c) and 2(d)], we only see a decrease of both conversion efficiencies by increasing the chemical potential. The power flow distributions at $\mu_c = 0$ and 0.5 eV are shown in Figs. 6(c) and 6(d), respectively. We note that they exhibit the same feature, i.e., the power flow ends up in waveguide-1 as a result of the trajectories on the Riemann sheets [see the yellow and white lines in Fig. 2(d)].

From now on, we only consider x polarized modes. The switching functionality is achieved by operating the device to work in two conditions, i.e., $\mu_c = 0$ (condition I) and 0.5 eV (condition II), with the power finally flowing to waveguide-1 and waveguide-2, respectively. These two values of chemical potential are often used for terahertz device design [49] and can be achieved experimentally [50]. We investigate the dependence of the device performance on the system parameters. We first calculate the conversion efficiencies as a function of the system length with other system parameters the same as those in Fig. 4. The results for conditions I and II are plotted in Figs. 7(a) and 7(b), respectively, where the dashed

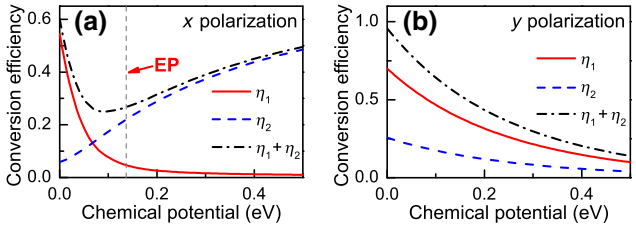

FIG. 5. Calculated conversion efficiencies $\eta_1 = P_1/P_0$ and $\eta_2 = P_2/P_0$ of the terahertz switch for (a) x polarized modes and (b) y polarized modes as a function of the chemical potential. The dashed line in (a) marks the position of the EP with $\mu_{c,\mathrm{EP}} = 0.143$ eV.

lines mark the device with $L = 60$ mm. The energy surfaces remain the same when varying the system length, but the length of the device affects the adiabaticity of the system. This is especially important for condition I where the state needs to get onto the higher-loss sheet [see Fig. 7(a)]. When the system is too short (e.g., $L = 10$ mm), the wave does not have enough time to leave waveguide-2 so that η_2 still dominates the output. A system that is too long (e.g., $L = 80$ mm) is also not good since η_1 starts to drop because of the loss in graphene. On the other hand, the system length only affects η_2 for condition II since the state evolves only on the lower-loss sheet [see Fig. 7(b)]. Considering all these effects, the system length is chosen to be 60 mm in order to optimize performances for both conditions I and II.

Another key parameter is the width of the graphene stripe, which can manipulate the energy surfaces of the system. A wider graphene stripe induces higher loss. We show the calculated conversion efficiencies as a function of the graphene stripe width for conditions I and II in Figs. 7(c) and 7(d), respectively, where the dashed lines mark the device with $w = 0.1$ mm. We find the graphene width is important for condition II. A decrease in the width can push the EP to a larger $\mu_{c,\mathrm{EP}}$, since the amount of loss contrast has to balance the coupling between the two waveguides in order to reach the EP. The switch does not work if the graphene stripe is too narrow [see Fig. 7(d)]. In contrast, the switch always works in condition I. A narrower graphene stripe can even lead to a higher conversion efficiency because of the lower loss introduced [see Fig. 7(c)]. Considering the performance in both conditions, we choose $w = 0.1$ mm.

Figures 7(e) and 7(f) show the conversion efficiency as a function of the detuning parameter ΔW with $\mu_c = 0$ and 0.5 eV, respectively. We find that a small variation in ΔW only slightly affects the performance in condition I. Specifically, the detuning ΔW needs to be large enough to ensure that the eigenmodes at the starting/end points are symmetry-broken modes. The choice $\Delta W = 0.1$ mm

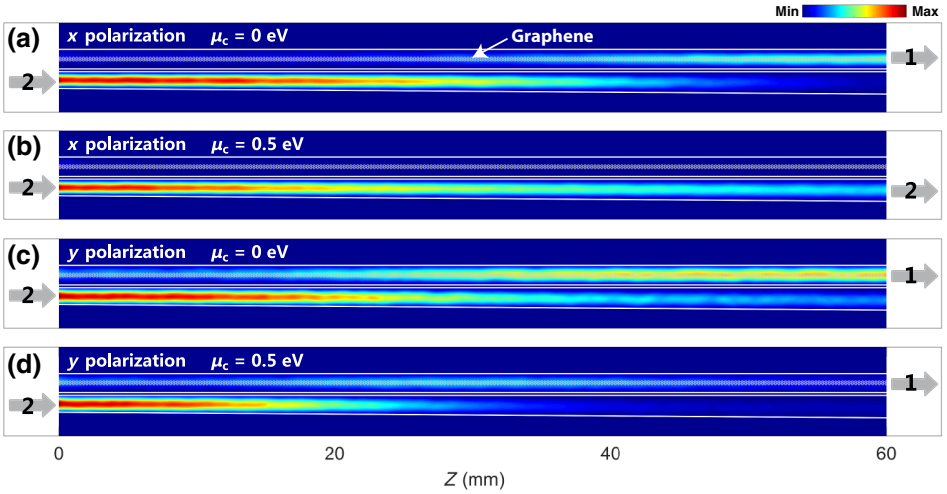

FIG. 6. Simulated z component power flow distributions in region II for x polarized modes with (a) $\mu_c = 0$ and (b) $\mu_c = 0.5$ eV. Items shown in (c) and (d) are the same as (a) and (b) except for the y polarized modes.

can meet this requirement. On the other hand, a large ΔW would require the system to be long enough for the sake of adiabaticity. As a result, the performance gets worse upon further increasing ΔW with a fixed system length of 60 mm. For condition II, the performance is almost insensitive to ΔW, since the eigenmodes are naturally symmetry-broken modes in the PT-broken phase region.

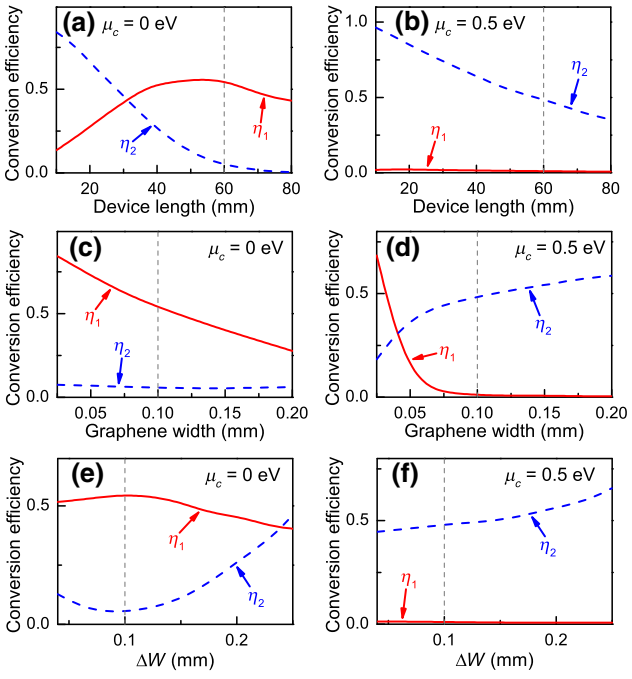

FIG. 7. Calculated conversion efficiencies of the terahertz switch for x polarized modes as a function of the device length with (a) $\mu_c = 0$ and (b) $\mu_c = 0.5$ eV. Items shown in (c) and (d) are the same as (a) and (b) except plotted as a function of the graphene width. Items shown in (e) and (f) are also the same except plotted as a function of the detuning. Other structural parameters are the same as those in Fig. 4. The dashed lines mark the optimized parameters which are also the choice in Fig. 4.

Other structural parameters such as the width/height of the waveguide are related to the working frequency. One can increase/decrease the waveguide size to make the system work at a lower/higher frequency.

We show how to obtain the optimized system parameters. In fact, the conversion efficiencies are $\eta_1 = 0.54$ and $\eta_2 = 0.05$ in condition I while they are $\eta_1 = 0.01$ and $\eta_2 = 0.49$ in condition II [see Fig. 5(a)]. This means in each working condition, nearly 50% of the injected power can reach the targeted waveguide in region III. Meanwhile, the power into the undesired waveguide is considerably lower than that injected into the targeted one. Since the working principle of the switch is based on loss-induced non-Hermiticity, power dissipations are inevitable, but there are ways to further improve the device performance. For condition I, one needs to minimize the loss of graphene at some chemical potential which can then help enhance the desired η_1. For condition II, one can choose a chemical potential as large as possible to make the system work in the deeper broken phase where the two eigenmodes are more localized. As a result, the desired η_2 would be enhanced since the wave experiences less dissipations when propagating in waveguide-2 [see Fig. 5(a)]. In experimental implementation, the switching speed will be limited by the response time of graphene, which is determined by the tuning schemes as well as the detailed structures [44]. A possible scheme is to use electrical gating to tune the proposed switch. The resistive-capacitive time constant can be expected to be on the order of ms considering the size of the waveguide system [39].

IV. CONCLUSION

In summary, we propose a design of a terahertz switch by employing the topological structure of the energy surfaces near an EP. The physics behind the design is that the transmission through the device is equivalent to the evolution of states along a trajectory on the Riemann sheets. By

tuning the chemical potential of graphene, we can manipulate the trajectory and therefore determine through which waveguide the power exits the system. We perform numerical simulations to optimize the device performance. Ways to further improve the efficiency are discussed. Previous 1×2 terahertz switches were typically achieved using a Y branch configuration [34,36,40] in which both branches are required to be tunable. In our design utilizing the physics of EPs, only one branch (i.e., waveguide-1) is attached to the tunable graphene which may help reduce power consumption due to the simplified device design. Although the switch is proposed at terahertz frequencies, the idea can, in principle, be applied to design devices working at other frequency ranges (e.g., optical communication frequency). Manipulating the trajectory on Riemann sheets of non-Hermitian systems can serve as a useful paradigm to design different types of devices.

ACKNOWLEDGMENTS

This work was supported by the Hong Kong Research Grants Council through Grant No. AoE/P-02/12. X.-L.Z. was also supported by the National Natural Science Foundation of China (Grant No. 61605056) and the China Postdoctoral Science Foundation (Grant No. 2016M591480). X.-B.W. was supported by the National Natural Science Foundation of China (Grant No. 61405070), China Postdoctoral Science Foundation (Grant No. 2016T90252), and Hong Kong Scholars Program (Grant No. XJ2016026).

[1] M. V. Berry, Physics of nonhermitian degeneracies, Czech. J. Phys. **54**, 1039 (2004).
[2] I. Rotter, A non-Hermitian Hamilton operator and the physics of open quantum systems, J. Phys. A **42**, 153001 (2009).
[3] N. Moiseyev, *Non-Hermitian Quantum Mechanics* (Cambridge University Press, Cambridge, 2011).
[4] W. D. Heiss, The physics of exceptional points, J. Phys. A **45**, 444016 (2012).
[5] W. D. Heiss, Repulsion of resonance states and exceptional points, Phys. Rev. E **61**, 929 (2000).
[6] C. Dembowski, H.-D. Gräf, H. L. Harney, A. Heine, W. D. Heiss, H. Rehfeld, and A. Richter, Experimental Observation of the Topological Structure of Exceptional Points, Phys. Rev. Lett. **86**, 787 (2001).
[7] T. Gao, E. Estrecho, K. Y. Bliokh, T. C. H. Liew, M. D. Fraser, S. Brodbeck, M. Kamp, C. Schneider, S. Höfling, Y. Yamamoto, F. Nori, Y. S. Kivshar, A. G. Truscott, R. G. Dall, and E. A. Ostrovskaya, Observation of non-Hermitian degeneracies in a chaotic exciton-polariton billiard, Nature **526**, 554 (2015).
[8] K. Ding, G. Ma, M. Xiao, Z. Q. Zhang, and C. T. Chan, Emergence, Coalescence, and Topological Properties of Multiple Exceptional Points and Their Experimental Realization, Phys. Rev. X **6**, 021007 (2016).
[9] J. Schnabel, H. Cartarius, J. Main, G. Wunner, and W. D. Heiss, PT-symmetric waveguide system with evidence of a third-order exceptional point, Phys. Rev. A **95**, 053868 (2017).
[10] A. Guo, G. J. Salamo, D. Duchesne, R. Morandotti, M. Volatier-Ravat, V. Aimez, G. A. Siviloglou, and D. N. Christodoulides, Observation of PT-Symmetry Breaking in Complex Optical Potentials, Phys. Rev. Lett **103**, 093902 (2009).
[11] K. G. Makris, R. EI-Ganainy, D. N. Christodoulides, and Z. H. Musslimani, Beam Dynamics in PT Symmetric Optical Lattices, Phys. Rev. Lett. **100**, 103904 (2008).
[12] A. Regensburger, C. Bersch, M. Miri, G. Onishchukov, D. N. Christodoulides, and U. Peschel, Parity-time synthetic photonic lattices, Nature **488**, 167 (2012).
[13] H. Benisty, A. Degiron, A. Lupu, A. D. Lustrac, S. Chénais, S. Forget, M. Besbes, G. Barbillon, A. Bruyant, S. Blaize, and G. Lérondel, Implementation of PT symmetric devices using plasmonics: Principle and applications, Opt. Express **19**, 18004 (2011).
[14] X. Zhu, H. Ramezani, C. Shi, J. Zhu, and X. Zhang, PT-symmetric acoustics, Phys. Rev. X **4**, 031042 (2014).
[15] L. Ge and A. D. Stone, Parity-Time Symmetry Breaking beyond One Dimension: The Role of Degeneracy, Phys. Rev. X **4**, 031011 (2014).
[16] B. Zhen, C. W. Hsu, Y. Igarashi, L. Lu, I. Kaminer, A. Pick, S. L. Chua, J. D. Joannopoulos, and M. Soljačić, Spawning rings of exceptional points out of Dirac cones, Nature **525**, 354 (2015).
[17] X. L. Zhang, S. B. Wang, W. J. Chen, and C. T. Chan, Exceptional points and symmetry recovery in a two-state system, Phys. Rev. A **96**, 022112 (2017).
[18] J. Doppler, A. A. Mailybaev, J. Böhm, U. Kuhl, A. Girschik, F. Libisch, T. J. Milburn, P. Rabl, N. Moiseyev, and S. Rotter, Dynamically encircling an exceptional point for asymmetric mode switching, Nature **537**, 76 (2016).
[19] S. Ke, B. Wang, C. Qin, H. Long, K. Wang, and P. Lu, Exceptional points and asymmetric mode switching in plasmonic waveguides, J. Lightw. Technol. **34**, 5258 (2016).
[20] A. U. Hassan, B. Zhen, M. Soljačić, M. Khajavikhan, and D. N. Christodoulides, Dynamically Encircling Exceptional Points: Exact Evolution and Polarization State Conversion, Phys. Rev. Lett. **118**, 093002 (2017).
[21] J. Wiersig, Enhancing the Sensitivity of Frequency and Energy Splitting Detection by Using Exceptional Points: Application to Microcavity Sensors for Singleparticle Detection, Phys. Rev. Lett. **112**, 203901 (2014).
[22] H. Hodaei, A. U. Hassan, S. Wittek, H. Garcia-Gracia1, R. El-Ganainy, D. N. Christodoulides, and M. Khajavikhan, Enhanced sensitivity at higher-order exceptional points, Nature **548**, 187 (2017).
[23] W. Chen, S. K. Özdemir, G. Zhao, J. Wiersig, and L. Yang, Exceptional points enhance sensing in an optical microcavity, Nature **548**, 192 (2017).
[24] A. Lupu, H. Benisty, and A. Degiron, Switching using PT symmetry in plasmonic systems: Positive role of the losses, Opt. Express **21**, 21651 (2013).
[25] A. Lupu, H. Benisty, and A. Degiron, Using optical PT-symmetry for switching applications, Photonics Nanostruct. Fundam. Appl. **12**, 305 (2014).

[26] S. Assawaworrarit, X. Yu, and S. Fan, Robust wireless power transfer using a nonlinear parity-time-symmetric circuit, Nature **546**, 387 (2017).
[27] B. Peng, S. K. Özdemir, S. Rotter, H. Yilmaz, M. Liertzer, F. Monifi, C. M. Bender, F. Nori, and L. Yang, Loss-induced suppression and revival of lasing, Science **346**, 328 (2014).
[28] P. Miao, Z. Zhang, J. Sun, W. Walasik, S. Longhi, N. M. Litchinitser, and L. Feng, Orbital angular momentum microlaser, Science **353**, 464 (2016).
[29] R. Fleury, D. L. Sounas, and A. Alù, Negative Refraction and Planar Focusing Based on Parity-Time Symmetric Metasurfaces, Phys. Rev. Lett. **113**, 023903 (2014).
[30] A. Leclerc, D. Viennot, G. Jolicard, R. Lefebvre, and O. Atabek, Exotic states in the strong-field control of H_2^+ dissociation dynamics: From exceptional points to zero-width resonances, J. Phys. B: At. Mol. Opt. Phys. **50**, 234002 (2017).
[31] I. Haritan, I. Gilary, Z. Amitay, and N. Moiseyev, Characteristic footprints of an exceptional point in the dynamics of Li dimer under a laser field, J. Chem. Phys. **143**, 154308 (2015).
[32] M. Tonouchi, Cutting-edge terahertz technology, Nat. Photonics **1**, 97 (2007).
[33] X. Cai, A. B. Sushkov, R. J. Suess, M. M. Jadidi, G. S. Jenkins, L. O. Nyakiti, R. L. Myers-Ward, S. Li, J. Yan, D. K. Gaskill, T. E. Murphy, H. D. Drew, and M. S. Fuhrer, Sensitive room-temperature terahertz detection via the photothermoelectric effect in graphene, Nat. Nanotechnol. **9**, 814 (2014).
[34] A. Vakil and N. Engheta, Transformation optics using graphene, Science **332**, 1291 (2011).
[35] J. Li, J. He, and Z. Hong, Terahertz wave switch based on silicon photonic crystals, Appl. Opt. **46**, 5034 (2007).
[36] K. Song and P. Mazumder, Active terahertz spoof surface plasmon polariton switch comprising the perfect conductor metamaterial, IEEE Trans. Electron. Devices **56**, 2792 (2009).
[37] H. Zhang, P. Guo, P. Chen, S. Chang, and J. Yuan, Liquid-crystal-filled photonic crystal for terahertz switch and filter, J. Opt. Soc. Am. B **26**, 101 (2009).
[38] H. M. Chen, J. Su, J. L. Wang, and X. Y. Zhao, Optically-controlled high-speed terahertz wave modulator based on nonlinear photonic crystals, Opt. Express **19**, 3599 (2011).
[39] M. Mittendorff, S. Li, and T. E. Murphy, Graphene-based waveguide-integrated terahertz modulator, ACS Photonics **4**, 316 (2017).
[40] M. Yarahmadi, M. K. Moravvej-Farshi, and L. Yousefi, Subwavelength graphene-based plasmonic THz switches and logic gates, IEEE Trans. Terahertz Sci. Technol. **5**, 725 (2015).
[41] Z. Li, Y. Zhang, and B. Li, Terahertz photonic crystal switch in silicon based on self-imaging principle, Opt. Express **14**, 3887 (2006).
[42] P. D. Cunningham, N. N. Valdes, F. A. Vallejo, L. M. Hayden, B. Polishak, X. H. Zhou, J. Luo, A. K. Y. Jen, J. C. Williams, and R. J. Twieg, Broadband terahertz characterization of the refractive index and absorption of some important polymeric and organic electro-optic materials, Appl. Phys. Lett. **109**, 043505 (2011).
[43] G. W. Hanson, Dyadic Green's functions and guided surface waves for a surface conductivity model of graphene, J. Appl. Phys. **103**, 064302 (2008).
[44] S. Yu, X. Wu, Y. Wang, X. Guo, and L. Tong, 2D materials for optical modulation: Challenges and opportunities, Adv. Mater. **29**, 1606128 (2017).
[45] A. W. Snyder and J. D. Love, *Optical Waveguide Theory* (Chapman and Hall, London, 1983).
[46] www.comsol.com.
[47] X. L. Zhang, S. B. Wang, B. Hou, and C. T. Chan, Dynamically encircling exceptional points: In situ control of encircling loops and the role of the starting point, Phys. Rev. X **8**, 021066 (2018).
[48] X. L. Zhang and C. T. Chan, Hybrid exceptional point and its dynamical encircling in a two-state system, Phys. Rev. A **98**, 033810 (2018).
[49] P. Y. Chen, C. Argyropoulos, and A. Alù, Terahertz antenna phase shifters using integrally-gated graphene transmission-lines, IEEE Trans. Antennas Propag. **61**, 1528 (2013).
[50] T. Jiang, D. Huang, J. Cheng, X. Fan, Z. Zhang, Y. Shan, Y. Yi, Y. Dai, L. Shi, K. Liu, C. Zeng, J. Zi, J. E. Sipe, Y. R. Shen, W. T. Liu, and S. Wu, Gate-tunable third-order nonlinear optical response of massless Dirac fermions in graphene, Nat. Photonics **12**, 430 (2018).